



Cite this: *Green Chem.*, 2023, **25**, 5872Received 6th May 2023,  
Accepted 12th July 2023

DOI: 10.1039/d3gc01486j

rsc.li/greenchem

## Selective electro-reforming of waste polyethylene terephthalate-derived ethylene glycol into C<sub>2</sub> chemicals with long-term stability†

Yuxiang Wang,<sup>a,b</sup> Kesheng Liu,<sup>a,b</sup> Fulai Liu,<sup>a</sup> Chuxuan Liu,<sup>a,b</sup> Rui Shi <sup>\*a</sup> and Yong Chen <sup>\*a,b</sup>

Electro-oxidation of ethylene glycol (EG) derived from polyethylene terephthalate (PET) into value-added C<sub>2</sub> products is essential for the electro-reforming of waste PET. However, achieving high selectivity and stability in the EG oxidation reaction (EGOR) remains a significant challenge. Herein, we successfully fabricated segregation-less Pd<sub>1</sub>Ag<sub>1</sub> alloy nanoparticles (NPs) that can be used for the electro-reforming of waste PET into glycolate C<sub>2</sub> products with high selectivity (97%) and long-term stability (>500 h). Electrochemical measurements and *in situ* Fourier-transform infrared spectroscopy (FTIR) results reveal that the addition of Ag atoms improves glycolate selectivity by reducing its adsorption on Pd active sites. In addition, the surface \*OH species generated on Ag sites facilitate the rapid oxidation of toxic carbonyl species, thereby improving the stability of Pd sites. Therefore, the synergistic effects of Pd<sub>1</sub>Ag<sub>1</sub> NPs provide an effective way for practical electro-reforming of real-world waste PET into value-added products with high selectivity and stability.

Accumulation of plastic waste has led to severe environmental concerns,<sup>1,2</sup> and there is an urgent need to develop effective methods for recycling end-of-life plastics. PET is a widely used polyester plastic,<sup>3,4</sup> and various physical and chemical recycling methods have been developed to recycle PET. Currently, approximately 90% of recycled PET is reclaimed through traditional mechanical recycling, but this approach often results in inferior properties of the reproduced materials compared to those of raw PET.<sup>5</sup> In contrast, chemical recycling methods involve the degradation of PET into monomers through hydrolysis,<sup>6</sup> methanolysis<sup>7</sup> and glycolysis,<sup>8</sup> followed by

repolymerisation to produce PET, which can enable closed-loop recovery. However, these methods are cost-ineffective.<sup>9</sup>

Recently, chemical recycling of PET through electro-reforming has received increasing attention.<sup>10–13</sup> The electro-oxidation of PET-derived ethylene glycol (EG) into value-added products that can be easily separated is a crucial step in this process. Several groups have reported the electro-reforming of PET-derived EG into C<sub>1</sub> products, such as carbonate and formate.<sup>10–17</sup> Compared to the deep oxidation to generate C<sub>1</sub> products, the controllable oxidation of EG into specific high-value C<sub>2</sub> products is more meaningful and also cost-effective. For instance, glycolic acid (GA) is an important industrial raw material that can be used as a monomer for the synthesis of biodegradable plastic polyglycolic acid.<sup>18</sup> However, the selective conversion of EG into GA is still challenging due to issues such as (i) the strong adsorption of intermediates on the Pd active sites, which reduces the selectivity of glycolate,<sup>19</sup> and (ii) the rapid deactivation of Pd-based catalysts during the electro-catalytic oxidation of alcohols caused by carbonyl species poisoning.<sup>20–23</sup> Researchers have attempted to address these challenges. For example, recent works have reported that Au or Pd nanoparticles loaded on Ni(OH)<sub>2</sub> substrates can convert PET into glycolate.<sup>24,25</sup> Shi and co-workers achieved the production of value-added GA by using PdAg/NF as the anode electro-catalyst.<sup>26</sup> However, the performance of the catalyst is still far from satisfactory. The rapid deactivation of the catalyst makes it unavailable for practical scenarios.

Herein, we report highly alloyed Pd<sub>1</sub>Ag<sub>1</sub> nanoparticles (NPs) as an efficient electrocatalyst for upcycling PET-derived EG into glycolate. The use of a strong reducing agent is crucial for fabricating a nanoparticle alloy, which exposes more surface Ag sites by avoiding segregation. Specifically, the addition of Ag atoms improves the selectivity and stability of Pd-based catalysts in the EGOR process by optimising the electronic structure and surface species. On the one hand, Ag atoms reduce the adsorption energy of glycolate on Pd sites, thus preventing unwanted over-oxidation and achieving high glycolate selectivity. On the other hand, Ag atom sites induce a large amount

<sup>a</sup>Key Laboratory of Photochemical Conversion and Optoelectronic Materials & CAS-HKU Joint Laboratory on New Materials, Technical Institute of Physics and Chemistry, Chinese Academy of Sciences, Beijing 100190, People's Republic of China. E-mail: shirui@mail.ipc.ac.cn, chen Yong@mail.ipc.ac.cn

<sup>b</sup>University of Chinese Academy of Sciences, Beijing 100049, People's Republic of China

† Electronic supplementary information (ESI) available. See DOI: <https://doi.org/10.1039/d3gc01486j>

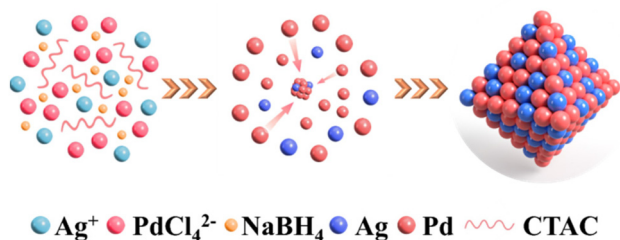
of \*OH active species to facilitate rapid oxidation of carbonyl species at the Pd active sites because of their high affinity with water,<sup>27,28</sup> and hence, this alleviates catalyst poisoning. Our results show that Pd<sub>1</sub>Ag<sub>1</sub> NPs demonstrate efficient electro-reforming of EG into glycolate with a high selectivity of 97% at 0.75 V vs. RHE. The electro-catalytic activity remains stable for over 500 h without attenuation. In a real two-electrode flow cell, the selectivity of glycolate is 91% when 52% of PET-derived EG is electro-reformed.

Pd<sub>x</sub>Ag<sub>y</sub> NPs were synthesised *via* the simultaneous reduction of H<sub>2</sub>PdCl<sub>4</sub> and AgNO<sub>3</sub> with ascorbic acid in CTAC aqueous solution at room temperature, as depicted in Scheme 1. The face-centred crystal structure of the resulting Pd<sub>x</sub>Ag<sub>y</sub> NPs was confirmed by X-ray diffraction (XRD). As shown in Fig. 1a, the diffraction peaks of Pd<sub>x</sub>Ag<sub>y</sub> nanoparticles were located between the peaks of pure Pd (PDF#46-1043) and pure Ag (PDF#89-3722). The diffraction peaks of Pd<sub>x</sub>Ag<sub>y</sub> NPs shifted from Pd to Ag as the Pd/Ag ratio decreased, indicating the formation of a Pd–Ag alloy structure rather than phase separation. X-ray photoelectron spectroscopy (XPS) was used to investigate the chemical environments of Pd and Ag (Fig. 1b and c). The binding energy of Pd 3d and Ag 3d in Pd<sub>1</sub>Ag<sub>1</sub> NPs shifted negatively compared to Pd and Ag binding energies, which is attributed to the electron transfer from Ag to Pd. These shifts are consistent with previous reports.<sup>29–32</sup> The Ag 3d<sub>5/2</sub> peak shift of Pd–Ag NPs prepared with NaBH<sub>4</sub> was more negative than that prepared with ascorbic acid (Fig. S1a†). This stronger electron transfer implies an increase in the Ag–Pd coordination number, *i.e.*, a higher dispersion.<sup>33</sup> Furthermore, to study the influence of Pd–Ag interaction on the electronic structure, the d-band centres of Pd/C and Pd<sub>1</sub>Ag<sub>1</sub> NPs were evaluated using surface valence band photoemission spectra. Pd<sub>1</sub>Ag<sub>1</sub> NPs showed an obvious negative shift compared with Pd/C (−4.72 eV vs. −4.21 eV) (Fig. S1b†).<sup>34</sup> Such a downshift of the d-band centre implies a relatively weak adsorption of the reaction intermediate on Pd sites,<sup>32,35–37</sup> which is beneficial for the selective conversion of EG into C<sub>2</sub> products. The actual Pd/Ag molar ratio of the samples was quantified using inductively coupled plasma optical emission spectrometry (ICP-OES) (Table S1†). The calculated molar ratio of Pd to Ag is essentially the same as the stoichiometry in the synthesis. Scanning electron microscopy (SEM) images showed that the Pd<sub>1</sub>Ag<sub>1</sub> alloy NPs had an average size of 20 nm (Fig. 1d). High-resolution transmission electron microscopy (HRTEM) examination

revealed that the lattice fringes of Pd<sub>1</sub>Ag<sub>1</sub> NPs exhibited interplanar spacings of 0.233 and 0.196 nm in the particle, corresponding to the (111) and (200) planes of the face-centred cubic Pd<sub>1</sub>Ag<sub>1</sub> alloy (Fig. 1e). No defects and lattice changes were observed in the clear lattice images, indicating that segregation was prevented. Energy-dispersive X-ray elemental maps confirmed that Pd and Ag elements were evenly distributed throughout the Pd<sub>1</sub>Ag<sub>1</sub> NP structure (Fig. 1f). Collectively, these results indicate the successful synthesis of a Pd–Ag NP alloy structure.

Prior to the electro-reforming process, PET was hydrolysed into terephthalate (TPA) and EG in an alkaline solution. As TPA precipitates in strong alkaline solutions, the electro-oxidation of EG was examined as a model reaction *via* a simple three-electrode system. The electrochemically active surface area (ECSA) of Pd<sub>x</sub>Ag<sub>y</sub> NPs and commercial Pd/C was evaluated through the reduction process of Pd oxides, and the results are presented in Table S1.† The ECSA of Pd<sub>x</sub>Ag<sub>y</sub> NPs was found to be slightly less than that of commercial Pd/C. To investigate the catalytic ability of Pd<sub>x</sub>Ag<sub>y</sub> NPs and commercial Pd/C toward EG oxidation, cyclic voltammetry (CV) curves were recorded in 1 M KOH and 1 M EG. The electro-catalytic current was normalised with respect to the mass of Pd (Fig. 2a) since the EGOR activity of Ag is negligible in this potential range (Fig. S2†). The pronounced anodic peaks in the forward and backward sweeps at 0.85 V and 0.65 V vs. RHE were attributed to oxidation of EG and other intermediate species, respectively. The current density of different compositions normalized with the carbon glass area and ECSA showed similar peaks (Fig. S3†). The Pd/Ag ratio of 1 : 1 exhibited the best EGOR performance (Fig. 2b), with the highest peak current of 1.36 A mg<sub>Pd</sub><sup>−1</sup>, which was substantially larger than that of Pd/C (0.55 A mg<sub>Pd</sub><sup>−1</sup>). Despite the smaller ECSA of Pd<sub>1</sub>Ag<sub>1</sub> NPs compared to commercial Pd/C, they exhibited higher intrinsic catalytic activity than Pd/C (Fig. S3†). To better understand the reason for this high activity, the Tafel slope and electrochemical impedance spectra were measured. The lower Tafel slope of Pd<sub>1</sub>Ag<sub>1</sub> NPs (118.5 mV dec<sup>−1</sup>) than that of commercial Pd/C (153.5 mV dec<sup>−1</sup>) illustrates efficient catalytic performance (Fig. 2c). Meanwhile, the Pd<sub>1</sub>Ag<sub>1</sub> NPs present a smaller charge transfer resistance (*R*<sub>ct</sub>) than commercial Pd/C, which is also favourable for interfacial electron transfer kinetics during EGOR (Fig. 2d).

Poor stability is a major challenge in the electro-reforming of PET. To assess the stability of the catalysts, chronoamperometry (CA) measurements were conducted in a mixture of 1 M KOH and 1 M EG for 3600 s. As shown in Fig. 3a, the current densities of both catalysts decreased rapidly at the beginning of the stability test, mainly because of the adsorption and accumulation of Pd oxides on the active site surface.<sup>38</sup> The Pd<sub>1</sub>Ag<sub>1</sub> NPs retained 83% of their initial mass activity after 3600 s at 0.85 V vs. RHE, which is considerably better than that of commercial Pd/C. Moreover, a comparison of the performance of other catalysts with that of the proposed catalysts is presented in Table S2;† the results show that the stability of Pd<sub>1</sub>Ag<sub>1</sub> NPs in the EGOR process is superior to that of all reported Pd-based alloy catalysts in the literature. To investi-



Scheme 1 PdAg NP synthesis in CTAC aqueous solution.

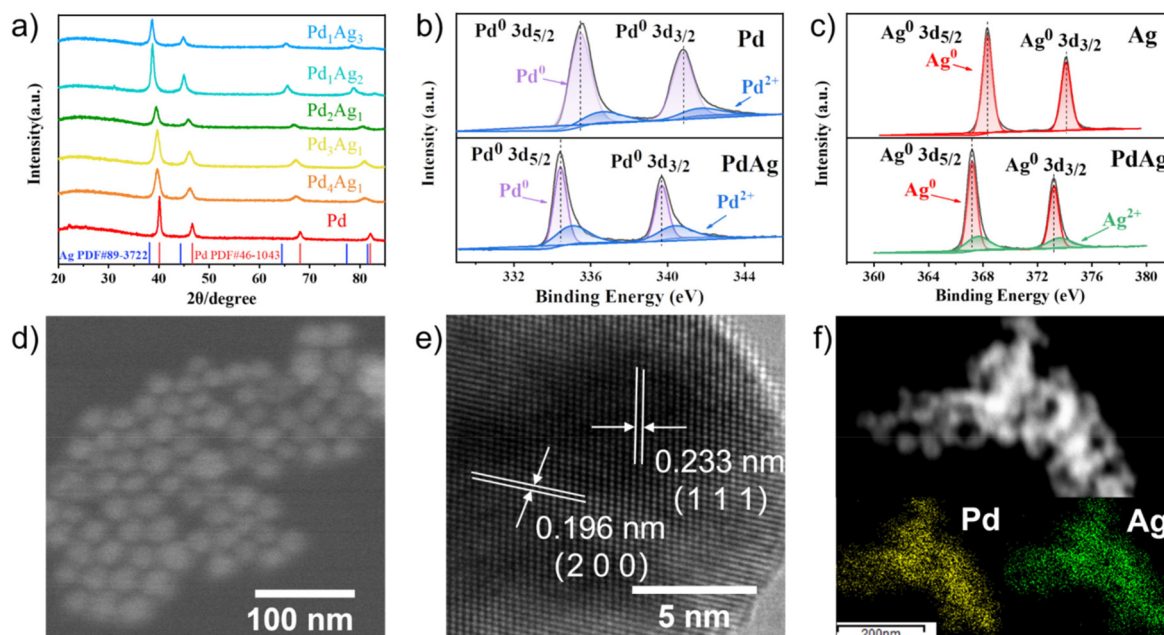


**Fig. 1** (a) XRD patterns of  $\text{Pd}_x\text{Ag}_y$  NPs. High-resolution XPS spectra of (b) Pd 3d and (c) Ag 3d. (d) SEM, (e) HRTEM and (f) mapping images of  $\text{Pd}_1\text{Ag}_1$  NPs.

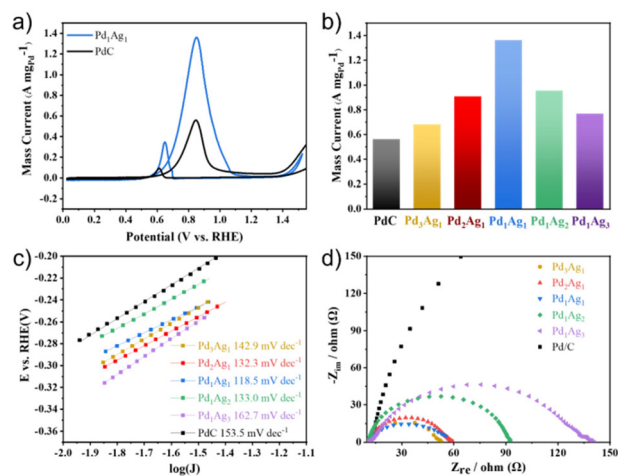


**Fig. 2** (a) CVs of  $\text{Pd}_1\text{Ag}_1$  NPs and commercial Pd/C in 1 M KOH and 1 M EG solution at  $10 \text{ mVs}^{-1}$ ; (b) comparison of peak mass currents of  $\text{Pd}_x\text{Ag}_y$  NPs and commercial Pd/C; (c) Tafel slope plots and (d) Nyquist plots of  $\text{Pd}_x\text{Ag}_y$  NP samples and commercial Pd/C in 1 M KOH containing 1 M EG.

gate the origin of this improved stability, CO anti-poisoning experiments were conducted (Fig. 3b and c). Compared to commercial Pd/C, the anodic wave belonging to the electro-oxidation of adsorbed CO into  $\text{CO}_2$  on the  $\text{Pd}_1\text{Ag}_1$  NP surface shifted to a lower potential, indicating that carbonyl species were more easily oxidised on the  $\text{Pd}_1\text{Ag}_1$  NP surface. Furthermore, we conducted electrochemical *in situ* FTIR measurements, and the corresponding binding assignments are provided in Table S3.† As shown in Fig. 3d, clear signals of

carbonyl species can be detected on the Pd/C surface in all potential ranges. However, the characteristic peak of CO on the  $\text{Pd}_1\text{Ag}_1$  NP surface was barely detectable (Fig. 3e), indicating that the oxidation of carbonyl species was enhanced within this potential range.

Furthermore, our findings show that the stability of  $\text{Pd}_1\text{Ag}_1$  NPs varies significantly in different voltage ranges (Fig. 3f). Specifically, the current density decreased to below 40% after 3600 s of the EGOR process, when the potential was less than 0.75 V. However, it remains above 75% when the potential was within the range of 0.75–1.05 V, with the highest stability (83%) observed at 0.85 V. Conversely, when the voltage exceeded 1.1 V, the catalyst deactivated rapidly (Fig. S4†). To clarify this point, we monitored the formation of  $^*\text{OH}$  species by an electrochemical method to reveal the rapid oxidation mechanism of carbonyl species. As shown in Fig. S5,†  $^*\text{OH}$  species were detected within the 0.75–1.05 V vs. RHE range; additionally, high stability was also observed in this range. These results provide evidence that the production of  $^*\text{OH}$  species was positively correlated with the stability of the catalyst. Specifically, since Ag atoms possess higher affinity with water than EG (Fig. S6†), the  $^*\text{OH}$  species generated at Ag sites provide highly reactive oxygen species for the rapid oxidation of carbonyl species,<sup>35</sup> thus preventing the poisoning of the Pd active sites (Fig. 3g). At low potentials (<0.75 V vs. RHE), the generation of adequate  $^*\text{OH}$  on Ag sites was difficult, which leads to the accumulation of carbonyl species on Pd active sites and catalyst poisoning. At a potential of 1.1 V vs. RHE, Ag was oxidised to  $[\text{Ag}(\text{OH})_2]_{\text{ads}}^-$ , which was adsorbed onto the catalyst surface, resulting in catalyst deactivation.<sup>39,40</sup> After comprehending the properties associated with the stability of

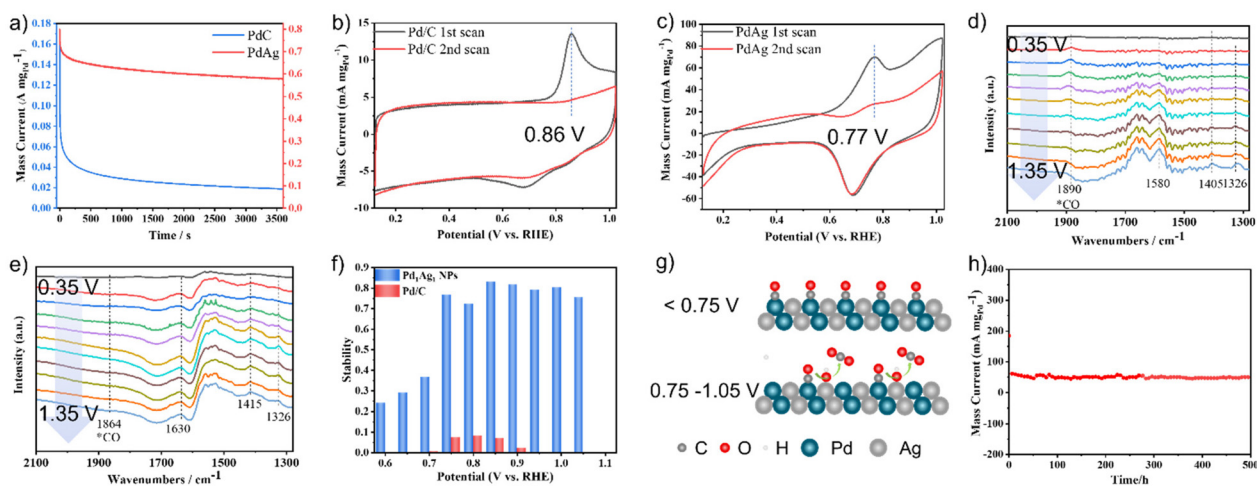


**Fig. 3** (a) Stability test for Pd<sub>1</sub>Ag<sub>1</sub> NPs and Pd/C for the anodic EG oxidation at 0.85 V vs. RHE for 1 h. CO-stripping curves of (b) Pd/C and (c) PdAg NPs. (d) Comparison of Pd<sub>1</sub>Ag<sub>1</sub> NPs and Pd/C at different voltages for 1 h. *In situ* electrochemical FTIR spectra of (e) Pd/C and (f) Pd<sub>1</sub>Ag<sub>1</sub> NPs at different voltages in 1 M KOH containing 1 M EG. (g) Proposed anti-poisoning mechanism of Pd<sub>1</sub>Ag<sub>1</sub> NPs at different voltage ranges. (h) Chronopotentiometry test of Pd<sub>1</sub>Ag<sub>1</sub> NPs at 0.85 V vs. RHE under fluidic state.

Pd<sub>1</sub>Ag<sub>1</sub> NPs, a 500 h chronoamperometry experiment was conducted at 0.85 V vs. RHE under fluidic state. The result revealed that 0.1 mg of Pd<sub>1</sub>Ag<sub>1</sub> NPs dispersed on a carbon cloth could maintain a current of 50–60 mA mg<sub>Pd</sub><sup>-1</sup> without attenuation (Fig. 3h). Moreover, TEM and HRTEM images confirm that the morphology of Pd<sub>1</sub>Ag<sub>1</sub> NPs is well maintained after long-term electro-reforming (Fig. S7†).

Nuclear magnetic resonance (NMR) spectra were obtained to identify the intermediates and products during EG oxidation. The <sup>1</sup>H NMR and <sup>13</sup>C NMR spectra (Fig. 4a and b) showed that glycolate is the main product with a selectivity of 97% at 0.75 V vs. RHE. At the same time, the carbonate formed by further oxidation of glycolate can be observed from <sup>13</sup>C NMR spectra. In addition, no other by-products (*e.g.* formate and oxalate) were detected (Fig. S8†). The selectivity of

glycolate was also investigated at different voltages. The results show that when the conversion of EG was about 50%, the selectivity of glycolate was more than 90% in the range of 0.7–0.85 V vs. RHE (Fig. 4c and S9†). *In situ* FTIR spectroscopy was used to investigate the origin of the high selectivity of glycolate (Fig. 3d and e). The blue-shift of the characteristic wavenumber of glycolate in Pd<sub>1</sub>Ag<sub>1</sub> NPs (1415 cm<sup>-1</sup>) compared to commercial Pd/C (1405 cm<sup>-1</sup>) indicates a relatively weak adsorption of glycolate,<sup>41</sup> which indicates limited deep oxidation and improved selectivity of glycolate.<sup>26</sup> Furthermore, this result is supported by the negative shift of the d-band centre in Pd<sub>1</sub>Ag<sub>1</sub> NPs (−4.72 eV) compared with Pd/C (−4.21 eV) (Fig. S1†), suggesting that the addition of Ag atoms can fine-tune the electronic structure to reduce the glycolate adsorption energy and improve glycolate selectivity.

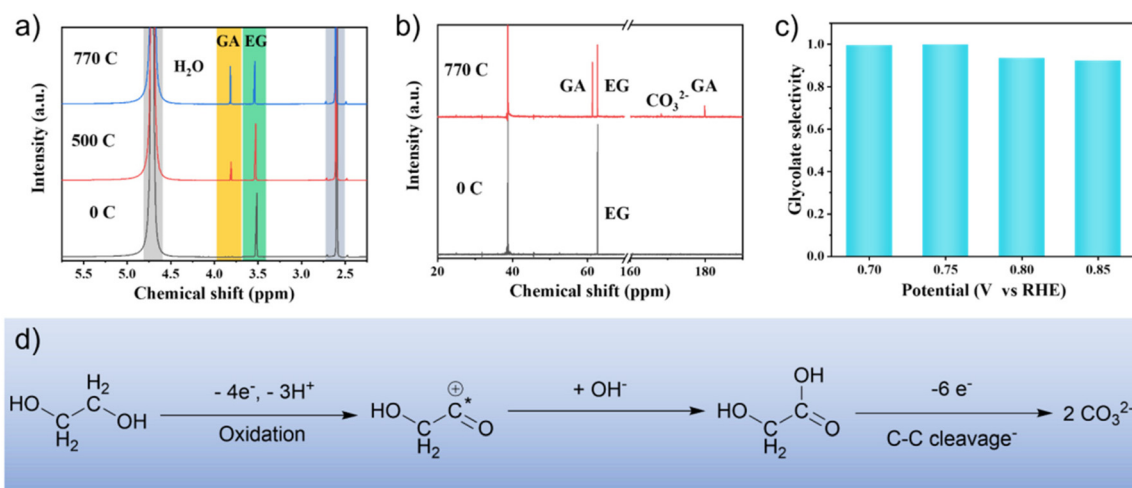


**Fig. 4** (a) <sup>1</sup>H NMR and (b) <sup>13</sup>C NMR spectra of the electrolyte at different Coulomb quantities. (c) Electro-oxidation selectivity of EG to glycolate at different voltages. (d) Reaction pathways of EG electro-oxidation on Pd<sub>1</sub>Ag<sub>1</sub> NPs.

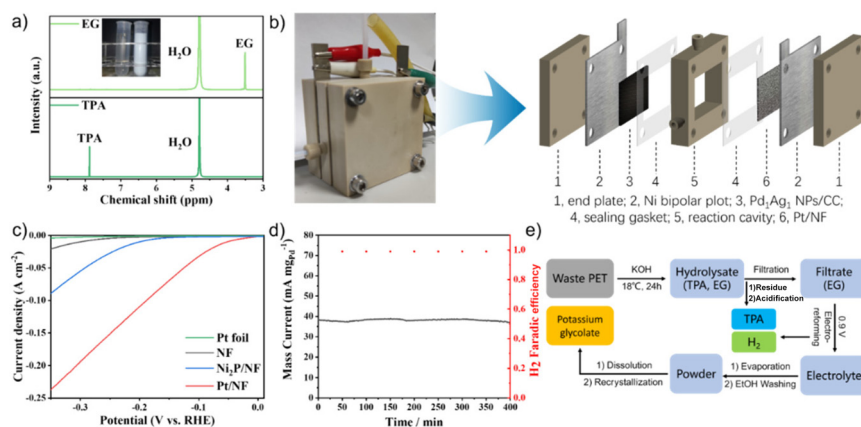


**Fig. 5** (a)  $^1\text{H}$  NMR spectra of the hydrolysate and TPA from green plastic bottles. Inset: images of the hydrolysate and TPA powder. (b) Images and schematic of a two-electrode flow cell reactor. (c) HER linear sweep voltammety curves for various materials in PET hydrolysates. (d)  $I$ - $T$  curves and faradaic efficiency of  $\text{H}_2$  of waste PET plastic hydrolysate in a flow cell reactor. (e) Schematic of electro-reforming of PET and product separation.

Moreover, *in situ* FTIR can also reveal the mechanism of the EGOR process. A vibration peak at  $1630\text{ cm}^{-1}$  was detected on the surface of  $\text{Pd}_1\text{Ag}_1$  NPs, corresponding to the adsorbed 2-hydroxyethyl intermediate, which further transforms into glycolate (Fig. 3d).<sup>42,43</sup> Based on the above results, a plausible pathway for EG oxidation was proposed, as shown in Fig. 4d. Initially, EG undergoes oxidative dehydrogenation at the surface to form adsorbed 2-hydroxyethyl species, which then combine with hydroxyl groups to generate glycolate. Finally, a small amount of glycolate undergoes C-C cleavage to form carbonate.

To evaluate the feasibility of electro-reforming of PET, colourless, blue and green plastic bottles were selected as raw materials for hydrolysis. The separated pure EG and TPA were characterised using  $^1\text{H}$  NMR spectra (Fig. 5a and S10<sup>†</sup>). TPA with a purity of 99.5% and a yield of 98% was obtained through the acidification of the filter residue of PET hydrolysis products. The  $\text{Pd}_1\text{Ag}_1$  NPs were then used as the anode to electrochemically reform the hydrolysate of real-world PET bottles in a flow cell (Fig. 5b). Nickel foam (NF) loaded with Pt NPs ( $\text{Pt}/\text{NF}$ ) was chosen as the cathode based on a comparison of the hydrogen evolution reaction (HER) overpotential (Fig. 5c). The current density was stabilised at  $40\text{ mA mg}_{\text{Pd}}^{-1}$  during 400 min of continuous electrolysis at a cell voltage of 0.9 V (Fig. 5d). The  $^1\text{H}$  NMR spectra revealed that the conversion rate of EG was 52% and the selectivity of glycolate was 91% (Fig. S11<sup>†</sup>).

To purify glycolate, the powder collected by evaporating the electrolyte was cleaned with EtOH, affording high-purity potassium glycolate crystals by dissolving in deionised water and recrystallising in EtOH (Fig. 5e). GC analysis of the cathode gas products obtained using the drainage method showed that only hydrogen was produced during the conversion of EG; moreover, the faradaic efficiency was >99% (Fig. 5d). These results demonstrate the feasibility of  $\text{Pd}_1\text{Ag}_1$  NPs for the industrial electro-reforming application of PET.

## Conclusions

In conclusion, this study demonstrates the successful upcycling of PET-derived EG into glycolate with high selectivity (>90%) and long-term stability (>500 h) through an alloying strategy to fine-tune the surface species and electronic structure of Pd sites. The incorporation of Ag sites on the surface of segregation-less  $\text{Pd}_1\text{Ag}_1$  NPs induces the formation of  $^*\text{OH}$  surface species, which enhances the stability of Pd active sites. Additionally, *in situ* FTIR and valence band spectra reveal the weak adsorption of glycolate on the catalyst due to the optimised d-band centre, leading to improved glycolate selectivity. This work not only presents a promising approach for the controlled oxidation of polyhydric alcohols but also opens up new avenues for the design of highly stable Pd-based catalysts for electro-reforming applications of PET.

## Author contributions

R. S. and Y. C. conceived the idea, planned the synthesis, and analysed the results. Y. W. performed the experiments. Y. W. and R. S. co-wrote the paper. K. L., F. L. and C. L. helped in analyzing the materials. All the authors discussed the results and contributed to the manuscript.

## Conflicts of interest

There are no conflicts to declare.

## Acknowledgements

We acknowledge the financial support from the National Key Research and Development Program of China (2022YFB3803600) and the Natural Science Foundation of China (21971250). Y. C. acknowledges the financial support

from the CAS-Croucher Funding Scheme for Joint Laboratories. F. L. thanks the Project funded by the China Postdoctoral Science Foundation (2022M723227).

## References

- 1 L. E. Revell, P. Kuma, E. C. Le Ru, W. R. C. Somerville and S. Gaw, *Nature*, 2021, **598**, 462–467.
- 2 D. K. Barnes, F. Galgani, R. C. Thompson and M. Barlaz, *Philos. Trans. R. Soc., B*, 2009, **364**, 1985–1998.
- 3 W. T. S. Huck, *Nature*, 2011, **472**, 425–426.
- 4 A. Rahimi and J. Garcia, *Nat. Rev. Chem.*, 2017, **1**, 0046.
- 5 K. Ragaert, L. Delva and K. Van Geem, *Waste Manage.*, 2017, **69**, 24–58.
- 6 T. Yoshioka, T. Sato and A. Okuwaki, *J. Appl. Polym. Sci.*, 1994, **52**, 1353–1355.
- 7 H. Kurokawa, M.-A. Ohshima, K. Sugiyama and H. Miura, *Polym. Degrad. Stab.*, 2003, **79**, 529–533.
- 8 L. Wang, G. A. Nelson, J. Toland and J. D. Holbrey, *ACS Sustainable Chem. Eng.*, 2020, **8**, 13362–13368.
- 9 X. Jiao, K. Zheng, Z. Hu, S. Zhu, Y. Sun and Y. Xie, *Adv. Mater.*, 2021, **33**, 2005192.
- 10 H. Zhou, Y. Ren, Z. Li, M. Xu, Y. Wang, R. Ge, X. Kong, L. Zheng and H. Duan, *Nat. Commun.*, 2021, **12**, 4679.
- 11 J. Wang, X. Li, T. Zhang, Y. Chen, T. Wang and Y. Zhao, *J. Phys. Chem. Lett.*, 2022, **13**, 622–627.
- 12 F. Liu, X. Gao, R. Shi, E. C. M. Tse and Y. Chen, *Green Chem.*, 2022, **24**, 6571–6577.
- 13 J. Wang, X. Li, M. Wang, T. Zhang, X. Chai, J. Lu, T. Wang, Y. Zhao and D. Ma, *ACS Catal.*, 2022, **12**, 6722–6728.
- 14 F. H. Ma, S. H. Wang, X. Q. Gong, X. L. Liu, Z. Y. Wang, P. Wang, Y. Y. Liu, H. F. Cheng, Y. Dai, Z. K. Zheng and B. B. Huang, *Appl. Catal., B*, 2022, **307**, 121198.
- 15 X. Liu, Z. Fang, X. Teng, Y. Niu, S. Gong, W. Chen, T. J. Meyer and Z. Chen, *J. Energy Chem.*, 2022, **72**, 432–441.
- 16 X. Li, J. Y. Wang, T. Zhang, T. F. Wang and Y. X. Zhao, *ACS Sustainable Chem. Eng.*, 2022, **10**, 9546–9552.
- 17 R. Shi, K. S. Liu, F. Liu, X. Yang, C. C. Hou and Y. Chen, *Chem. Commun.*, 2021, **57**, 12595–12598.
- 18 K. Budak, O. Sogut and U. Aydemir Sezer, *J. Polym. Res.*, 2020, **27**, 208.
- 19 J. L. Lin, J. Ren, N. Tian, Z. Y. Zhou and S. G. Sun, *J. Electroanal. Chem.*, 2013, **688**, 165–171.
- 20 H. Xu, B. Yan, K. Zhang, J. Wang, S. Li, C. Wang, Y. Shiraiishi, Y. Du and P. Yang, *J. Alloys Compd.*, 2017, **723**, 36–42.
- 21 J. J. Lv, L. P. Mei, X. Weng, A. J. Wang, L. L. Chen, X. F. Liu and J. J. Feng, *Nanoscale*, 2015, **7**, 5699–5705.
- 22 R. Jana, U. Subbarao and S. C. Peter, *J. Power Sources*, 2016, **301**, 160–169.
- 23 J. Qi, N. Benipal, C. Liang and W. Li, *Appl. Catal., B*, 2016, **199**, 494–503.
- 24 Y. Yan, H. Zhou, S. M. Xu, J. Yang, P. Hao, X. Cai, Y. Ren, M. Xu, X. Kong, M. Shao, Z. Li and H. Duan, *J. Am. Chem. Soc.*, 2023, **145**(11), 6144–6155.
- 25 F. Liu, X. Gao, R. Shi, Z. Guo, E. C. M. Tse and Y. Chen, *Angew. Chem., Int. Ed.*, 2023, **62**, e202300094.
- 26 B. X. Di Si, L. Chen and J. Shi, *Chem Catal.*, 2021, **1**, 941–955.
- 27 L. Guillemot and K. Bobrov, *Surf. Sci.*, 2007, **601**, 871–875.
- 28 J. Qian, Y. Ye, H. Yang, J. Yano, E. J. Crumlin and W. A. Goddard 3rd, *J. Am. Chem. Soc.*, 2019, **141**, 6946–6954.
- 29 J. A. Zamora Zeledon, M. B. Stevens, G. Gunasooriya, A. Gallo, A. T. Landers, M. E. Kreider, C. Hahn, J. K. Norskov and T. F. Jaramillo, *Nat. Commun.*, 2021, **12**, 620.
- 30 D. A. Slanac, W. G. Hardin, K. P. Johnston and K. J. Stevenson, *J. Am. Chem. Soc.*, 2012, **134**, 9812–9819.
- 31 K. Mori, T. Sano, H. Kobayashi and H. Yamashita, *J. Am. Chem. Soc.*, 2018, **140**, 8902–8909.
- 32 Y. Jin, S. Sarina, H. Liu, W. Martens, E. R. Waclawik, E. Peiris, J. Jia, J. Shang, L. Kou, C. Guo and H.-Y. Zhu, *ACS Catal.*, 2022, **12**, 11226–11238.
- 33 M. Karatok, H. T. Ngan, X. Jia, C. R. O'Connor, J. A. Boscoboinik, D. J. Stacchiola, P. Sautet and R. J. Madix, *J. Am. Chem. Soc.*, 2023, **145**(9), 5114–5124.
- 34 Y. Qin, W. Zhang, F. Wang, J. Li, J. Ye, X. Sheng, C. Li, X. Liang, P. Liu, X. Wang, X. Zheng, Y. Ren, C. Xu and Z. Zhang, *Angew. Chem., Int. Ed.*, 2022, **61**, e202200899.
- 35 W. Huang, X. Kang, C. Xu, J. Zhou, J. Deng, Y. Li and S. Cheng, *Adv. Mater.*, 2018, **30**, 1706962.
- 36 L. Chen, L. Lu, H. Zhu, Y. Chen, Y. Huang, Y. Li and L. Wang, *Nat. Commun.*, 2017, **8**, 14136.
- 37 X. L. Cai, C. H. Liu, J. Liu, Y. Lu, Y. N. Zhong, K. Q. Nie, J. L. Xu, X. Gao, X. H. Sun and S. D. Wang, *Nano-Micro Lett.*, 2017, **9**, 48.
- 38 Q. Zhang, J. Weng and J. Xu, *J. Phys. Chem. C*, 2021, **125**, 18717–18724.
- 39 S. Abd El Rehim, H. Hassan, M. Ibrahim and A. Amin, *Monatsh. Chem.*, 1998, **129**, 1103–1117.
- 40 I. R. Zamora-Garcia, A. Alatorre-Ordaz, J. G. Ibanez, M. G. Garcia-Jimenez, Y. Nosaka, T. Kobayashi and S. Sugita, *Electrochim. Acta*, 2013, **111**, 268–274.
- 41 J.-H. Zheng, G. Li, J.-M. Zhang, N. Cheng, L.-F. Ji, J. Yang, J. Zhang, B.-W. Zhang, Y.-X. Jiang and S.-G. Sun, *Sci. China: Chem.*, 2022, **66**, 279–288.
- 42 H. Wang, B. Jiang, T.-T. Zhao, K. Jiang, Y.-Y. Yang, J. Zhang, Z. Xie and W.-B. Cai, *ACS Catal.*, 2017, **7**, 2033–2041.
- 43 L. Xin, Z. Zhang, J. Qi, D. Chadderton and W. Li, *Appl. Catal., B*, 2012, **125**, 85–94.